Invited Paper

Optimization of mid-IR Photothermal Imaging for Tissue Analysis

Atcha Totachawattana[a,b], Shyamsunder Erramilli[b,d,e], Michelle Y. Sander*[a,b,c]
[a]Department of Electrical and Computer Engineering, Boston University, 8 St. Mary's Street, Boston, MA, 02115, USA;
[b]Photonics Center, Boston University, 8 Street. Mary's St, Boston, MA, USA 02115;
[c]Division of Materials Science and Engineering, Boston University, 15 St. Mary's Street, Boston, MA, 02115;
[d]Department of Physics, Boston University, 590 Commonwealth Avenue, Boston, MA, 02115;
[e]Department of Biomedical Engineering, Boston University, 44 Cummington Street, Boston, MA, 02115;

ABSTRACT

Photothermal imaging in the mid-infrared enables highly sensitive, label-free microscopy by relying on bond-specific characterization of functional groups within the samples. In a pump-probe configuration, the mid-infrared (mid-IR) pump laser is tuned to characteristic vibrational modes and through localized absorption thermal changes in the refractive index are induced. The shorter wavelength probe scatter can be detected with lock-in technology, utilizing highly sensitive detectors at telecommunication wavelengths. This mitigates the need of complex detector technology as required for traditional infrared spectroscopy/Fourier Transform Infrared Spectroscopy.

The presented photothermal system integrates a high brightness quantum cascade laser that can be tuned continuously over a spectral range of interest with a fiber probe laser. Fiber laser technology features a compact footprint and offers robust performance metrics and reduced sensitivity to environmental perturbations compared to free-space laser configurations. In systematic spectroscopy studies where the probe laser parameters were modified, we demonstrate that the signal-to-noise ratio can be significantly enhanced by utilizing a mode-locked laser compared to a continuous-wave laser.

With a raster-scanning approach, photothermal spectroscopy can be extended to hyperspectral label-free mid-infrared imaging to combine spectral content with localized sample details. By tuning the pump laser to the amide-I absorption band around 1650 cm^{-1} in biological tissue samples, the spectral characteristics can provide insight into the secondary structure of proteins (e.g. amyloid plaques; alpha-helix, beta-sheet). We present the versatility of our mid-IR photothermal system by analyzing histopathological tissue sections of cancerous tissue in a non-contact, non-destructive approach with good sensitivity.

Keywords: Photothermal imaging, mid-infrared spectroscopy, hyperspectral imaging, ultrafast laser, fiber laser

1. INTRODUCTION

In recent years, there has been a growing interest in photothermal spectroscopy[1,2] as a label-free technique for molecule specific detection and characterization of samples. In photothermal spectroscopy, absorption of the pump laser light induces a change in the temperature and refractive index of the sample. In a pump-probe configuration, the probe beam scatter due to the change in refractive index is measured as the photothermal signal (PTS). High contrast photothermal imaging and single molecule detection with high signal-to-noise ratio (SNR) have been demonstrated in the visible and near-infrared regime[3–7].

The development of quantum cascade lasers (QCLs)[8] as a mid-infrared (mid-IR) source with high spectral brightness has opened new pathways for infrared spectroscopy[9,10] where a large number of characteristic resonances form the "fingerprint region". By extending photothermal spectroscopy into the mid-infrared[11–15], the inherent absorption of the characteristic normal and vibrational modes in the mid-IR can be used for contact-less and label-free identification of functional groups in molecules.

*msander@bu.edu

Ultrafast Nonlinear Imaging and Spectroscopy III, edited by Zhiwen Liu,
Proc. of SPIE Vol. 9584, 95840C · © 2015 SPIE · CCC code:
0277-786X/15/$18 · doi: 10.1117/12.2187652

In the presented mid-IR photothermal spectroscopy system, a tunable QCL pump laser is combined with an erbium-doped fiber laser (EDFL) probe at near-infrared (near-IR) wavelengths. The probe laser wavelength is chosen in an eye-safe wavelength regime that is removed from the strong infrared absorption bands. This allows for the use of commercially available, highly sensitive photodetectors at room temperature, compared to mid-IR detectors which usually require external cooling. The fiber probe power can be easily scaled by incorporating erbium-doped fiber amplifiers (EDFAs) in an all-fiber configuration, offering stable operation with reduced sensitivity to environmental perturbations. For this work, the customization and optimization of the fiber laser configuration are critical to achieve an overall enhanced photothermal spectroscopy system performance.

By combining the two classical fields of spectroscopy and microscopy, spatially resolved molecular and structural information can be analyzed, leading to hyperspectral imaging capabilities. Recently, this approach of infrared microspectroscopy has been applied to various fields, among them histopathology. For biological tissue characterization, the mid-IR spectral vibrational response can provide insight into the biomolecular composition of cell structures and conformational changes in the secondary structure of proteins[16–19]. In pathology, after tagging the tissue with exogenous biomarkers, some ambiguity during visual tissue inspection can remain. Providing biochemical and molecular composition combined with spatial localization can help uniquely identify between different disease and disease stages. Spectral characterization of the amide bands in proteins[20,21] and spectral shifts in their absorption bands can be linked to the secondary structure of proteins (amide-I band) in tissue, providing insight into cancer or neurodegenerative diseases.

In this work, we demonstrate that the SNR in photothermal spectroscopy can be enhanced by optimizing laser operating parameters. A high SNR that features an asymptotic behavior is demonstrated on a 6 µm-thick liquid crystal sample of 4-Octyl-4'-Cyanobiphenyl (8CB). Photothermal imaging is performed on a 50 µm-thick histopathological section of human prostate tumor tissue where the spectral absorption of the amide-I band is characterized. The images show good contrast and visualization of tissue, thus outlining the potential of photothermal microspectroscopy for the analysis of histopathological tissue.

2. EXPERIMENTAL SETUP

2.1 Photothermal setup

The experimental set-up for photothermal spectroscopy and imaging is shown in Figure 1. A quantum cascade laser, tunable from 1575 – 1745 cm^{-1} serves as the pump laser. The QCL is pulsed at 100 kHz with a pulse duration of 500 ns, corresponding to a 5% duty cycle. The EDFL probe operates in the near-IR and can be amplified in two consecutive stages of EDFAs. The pump and probe lasers are collinearly combined in a dichroic mirror, then focused onto the sample by a ZnSe objective lens with an NA of 0.25 and a focal length of 6 mm. The transmitted forward scatter of the probe beam is detected in a heterodyne scheme[22] by an amplified InGaAs photodetector and a low-noise voltage preamplifier. The PTS is isolated using a lock-in amplifier synchronized to the repetition rate of the QCL. All photothermal spectra and images are taken at 20 ºC under purged conditions to reduce water (<1 % relative humidity) and CO_2 absorption.

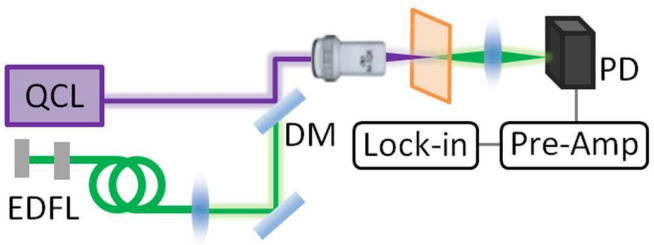

Figure 1. Experimental setup for photothermal spectroscopy and imaging. A quantum cascade laser (QCL) pump and erbium-doped fiber laser (EDFL) probe are collinearly combined at a dichroic mirror (DM). Both beams are focused by a ZnSe objective onto the sample. The probe beam forward scatter is detected at the photodetector (PD) and amplified by a low-noise voltage preamplifier. The PTS is isolated using a lock-in amplifier synchronized to the repetition rate of the QCL.

Figure 2 shows the two probe laser configurations studied in this work. Both lasers are formed by a linear laser cavity with either a semiconductor saturable Bragg reflector (SBR) or silver mirror butt-coupled to one end of the cavity, see Figure 2(a), (b). Self-starting ultrafast operation is initiated by a combination of soliton mode-locking with saturable absorption[23,24]. Figure 2(c) shows the optical spectrum of the ultrafast mode-locked laser (MLL), operating at a center wavelength of 1563 nm with a full-width half maximum bandwidth of 9.4 nm, corresponding to a transform-limited pulse duration of ~280 fs. The repetition rate is 1.04 GHz and output powers of 10 mW are obtained. The optical spectrum of the continuous wave (cw) laser is shown in Figure 2(d). The cw laser operates at a center wavelength of 1606 nm with a bandwidth of 0.85 nm. Up to 30 mW of cw output power is generated for 10 % output coupling for 400 mW of pump power. Both EDFLs are amplified by two stages of EDFAs.

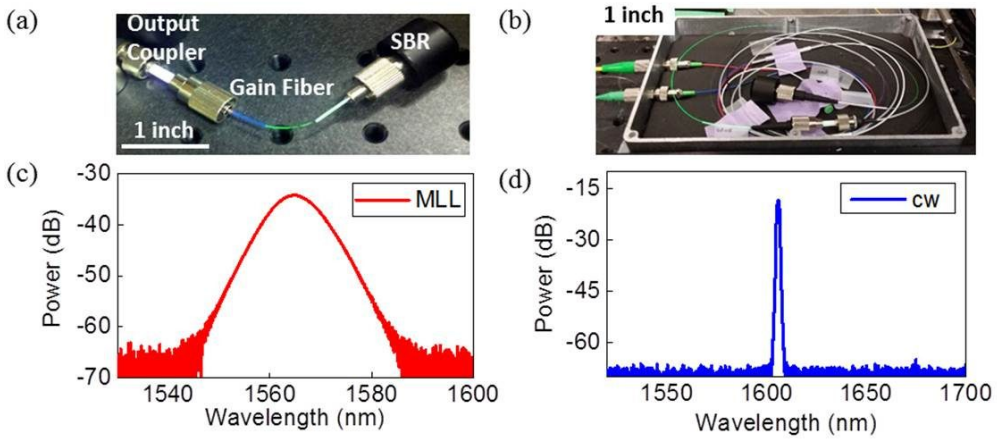

Figure 2. (a) An ultrafast mode-locked laser (MLL) with a repetition rate of 1.04 GHz. (b) A compact continuous wave (cw) EDFL in a box with dimensions of 4 x 7 inches. (c) Optical spectrum of the MLL operating at a center wavelength of 1563 nm with a bandwidth of 9.4 nm, corresponding to a transform-limited pulse duration of ~ 280 fs. (d) Optical spectrum of the cw laser operating at 1606 nm with a bandwidth of 0.85 nm

2.2 Experimental parameters

2.2.1. Photothermal spectroscopy

Photothermal spectra were measured by tuning the QCL wavenumber from 1580 to 1740 cm^{-1} in steps of 0.2 cm^{-1}. A liquid crystal 4-Octyl-4'-Cyanobiphenyl (8CB) was chosen for these studies because it features a well-characterized absorption spectra in the mid-infrared[25]. A 6 µm-thick 8CB liquid crystal layer was sandwiched between two CaF_2 windows with a 6 µm-thick Mylar spacer[24]. For the 8CB liquid crystal sample, 0.5 mW of pump power was incident onto the sample at the absorption maximum of the targeted C-H scissoring band at 1607 cm^{-1}.

2.2.2 Photothermal imaging

Tumors were grown from a subcutaneous inoculation of human prostate tumor cells (PC3-2G7) into nude mice. The tumors had an incubation period of 48 days and were fixated in formaldehyde then sectioned into 50 µm-thick sections. For photothermal spectroscopy and imaging of the tumor tissue, a probe power of 2.85 mW and a pump power of ~0.5 mW were incident on the sample. Photothermal images were obtained by raster scanning the sample with a step size of 1 µm with the pump laser fixed at a wavenumber of 1657 cm^{-1}. For cross-validation, optical images of the histopathological samples were taken using a Nikon stereo microscope (SMZ-800) with a 10x objective lens.

2.2.3 Fourier Transform Infrared Spectroscopy

A mid-infrared spectral measurement of the tumor sample was taken with a FTIR spectrometer (Nexus 670, Nicolet). The spectrum was taken with a resolution of 2 cm^{-1} under purged conditions to minimize water and CO_2 absorption.

3. EXPERIMENTAL RESULTS AND DISCUSSION

3.1 Analysis of photothermal signal-to-noise ratio

To determine the performance of the photothermal system, a study of the SNR was conducted on the liquid crystal sample. Photothermal spectra of the 6 µm-thick 8CB were measured with 0.5 mW of pump power incident on the sample and at varying probe powers. The measured photothermal spectra for a focused probe power of 1.4 mW on the sample plane are shown in Figure 3(a) for both the cw laser (blue triangles) and MLL (red circles). The characteristic C-H scissoring band at 1607 cm^{-1} of the 8CB liquid crystal is reproduced. Solid lines indicate a Gaussian fit to the measured data, which was collected in three spectral measurements. While the spectral parameters are identical in both cases, the PTS of 64.5 mV is higher by a factor of ~1.3 for the MLL compared to the cw laser PTS at 50.3 mV for the same probe power (compare Table 1). Thus, the maximum PTS as well as the background for a range of probe powers are recorded in Figure 3(b). The background is measured with the QCL beam blocked, corresponding to the directly transmitted probe beam power through the sample. As seen in Figure 3(b), the trajectory of the background with increasing probe power follows a linear relationship[26]. Solid lines in Figure 3(b) show a linear fit to the background value for the cw laser (blue triangles) and MLL (red circles) where the background for the MLL is significantly reduced compared to the cw laser. Thermal noise contributions as well as shot noise are expected be comparable for both lasers. The difference in background can be explained by the intrinsic intensity laser noise at the pump modulation frequency of 100 kHz, where overlap with relaxation oscillations in the cw laser lead to increased noise contributions.

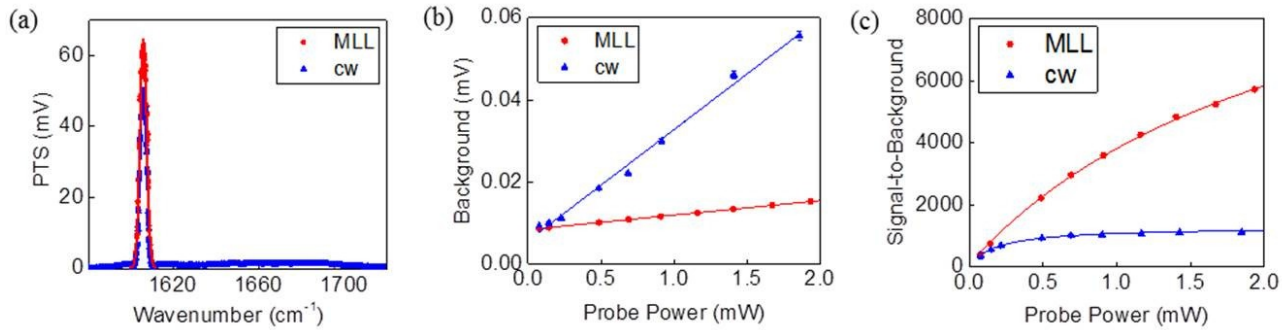

Figure 3. (a) Photothermal spectra of 8CB liquid crystal showing the C-H scissoring band with an absorption maximum at 1607 cm^{-1}. Both spectra are measured at a probe power of 1.4 mW incident onto the sample. Gaussian fits to the measured data are shown as solid lines for a mode-locked laser (MLL, red circles) and cw laser (blue triangles). (b) Background values at varying probe powers for the cw laser (blue triangles) and MLL (red circles). Solid lines are linear fits to background. (c) Corresponding SNR shown for the cw laser (blue triangles) and MLL (red circles). The solid lines are a fit to the measured data based on the linear fits to the maximum PTS and background. The highest measured SNR is 1,117 ± 34 and 6,761 ± 118 for the cw laser at 1.8 mW and the MLL at 2.7 mW, respectively.

The SNR, shown in Figure 3(c), was calculated by dividing the maximum PTS by the background value. At each probe power corresponding to the maximum PTS, background values were obtained by interpolation using a linear fit to the measured background values. The solid lines in Figure 3(c) are phenomenological fits to the data based on the slopes of the linear fits to the maximum PTS (44.6 mV/mW for MLL, 34.8 mV/mW for cw laser) and background values (0.0035 mV/mW for MLL, 0.0271 mV/mW for cw laser). The combination of reduced background for the ultrafast MLL with slightly enhanced PTS strengths results in a higher SNR than for the cw laser at comparable probe power values. At a probe power of 1.4 mW, the SNR of the MLL is 4,845 ± 84 compared to the cw laser which has a SNR of 1,104 ± 37. The highest measured SNR is 6,761 ± 118 at a probe power of 2.7 mW for the MLL and 1,117 ± 34 at a probe power of 1.8 mW for the cw laser. The comparison is summarized in Table 1.

Table 1. Comparison of cw and MLL performance at 1.4 mW of probe power incident on the 8CB liquid crystal sample.

	cw laser	**ultrafast MLL**
Maximum PTS (mV)	50.3 ± 4.9	64.5 ± 6.9
Background (mV)	$4.6 \times 10^{-2} \pm 1.1 \times 10^{-3}$	$1.3 \times 10^{-2} \pm 2.9 \times 10^{-4}$
SNR	1,104 ± 37	4,845 ± 84
Asymptotic Limit	1,282	12,605

The phenomenological model for the SNR based on the ratio of two linear equations indicates that there exists an asymptotic limit that characterizes the predictable maximum SNR for a given experimental configuration. In the presented setup, an asymptotic limit of 12,605 is predicted for the MLL compared to the cw laser with an asymptotic limit of 1,282, indicating an order of magnitude improvement in the SNR for the MLL and exceeding measured FTIR SNR values. The asymptotic limit implies a "law of diminishing returns" for higher probe powers. At the maximum power of 1.8 mW at the sample plane for the cw laser, 87 % of the asymptotic limit is reached and further increase in the probe power leads only to a marginal improvement in the SNR. However, the high SNR of the MLL for a probe power of 2.7 mW corresponds to 54 % of the asymptotic limit. The asymptotic limit therefore introduces a benchmark for photothermal spectroscopy performance as it relates each measured SNR to the best possible system performance. This analysis applies to any photothermal system that features linear dependence of the PTS and background with increasing probe powers. Based on only a few measurements, the asymptotic limit as the ratio between the PTS and background slopes can be experimentally determined in a straightforward manner, providing a powerful analysis metric.

3.2 Photothermal spectroscopy and imaging of tumor tissue

To investigate biological samples, a tumor tissue with a focus on the amide-I protein band was studied. Photothermal and FTIR spectra clearly resolve absorption of the amide-I band by the sample. The photothermal (blue squares) and FTIR spectra (black solid line) of the tumor tissue are shown in Figure 4(a) and Figure 4(b), respectively.

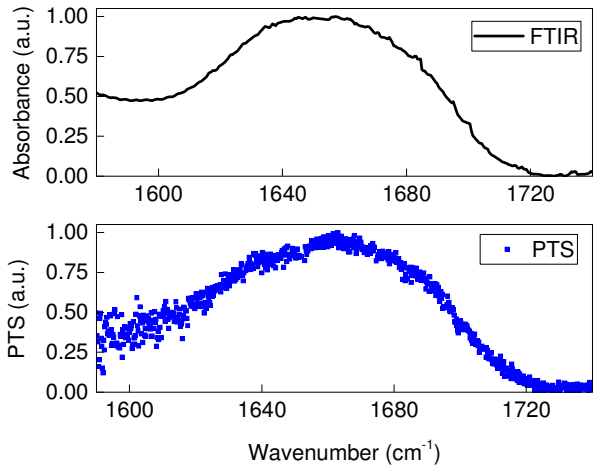

Figure 4. (a) FTIR spectrum of 50 µm-thick tumor tissue of the amide-I band. (b) Measured corresponding photothermal spectrum.

By targeting the peak of the absorption at 1657 cm^{-1} of the tumor tissue, a photothermal image of the tumor tissue was acquired. Photothermal images were obtained by raster-scanning over the sample with a step size of 1 µm. Figure 5(a) shows a false-color 480 µm x 480 µm photothermal image of the tumor tissue. The photothermal shows good co-registration with an optical microscope image of the corresponding area (unstained tissue), shown in Figure 5(b). In addition, local hotspots, indicating a high accumulation within the amide-I band that can be linked to cells are clearly spatially resolved. Hyperspectral images at different characteristic wavenumbers within the amide-I band can provide a quantitative measure through the spectral shape and absorption strength and consequently insights into the different secondary protein conformations. Thus, the potential for tissue characterization with photothermal spectroscopy has been shown. A detailed analysis with respect to pathology and comparison to stained tissue is currently ongoing.

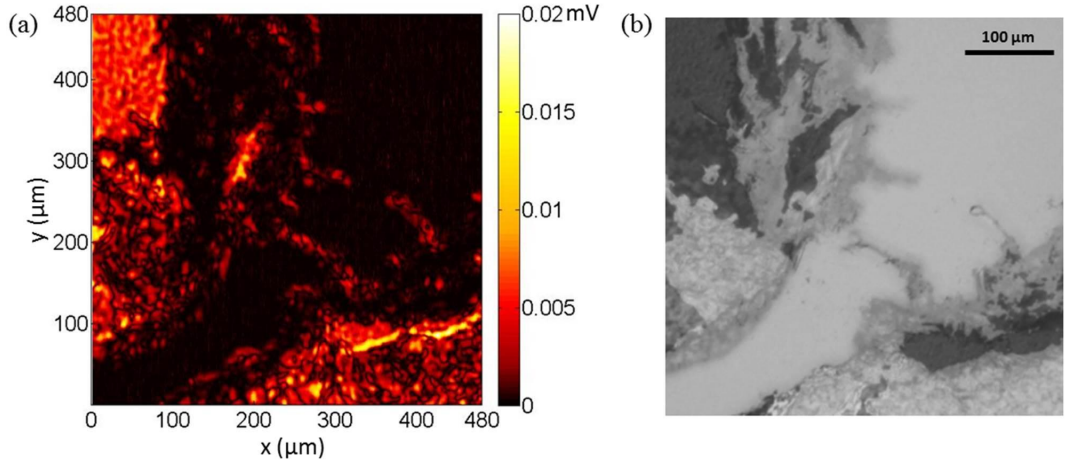

Figure 5. (a) Photothermal image of the tumor tissue. To obtain this 480 x 480 µm image, the sample was raster-scanned with a step size of 1 µm with a pump power of 0.5 mW at 1657 cm^{-1} and a probe power of 2.85 mW incident on the sample. (b) Optical microscope image of the corresponding area of the tumor tissue.

4. CONCLUSIONS

In this paper, we presented a mid-infrared photothermal spectroscopy system with enhanced sensitivity. Optimization of a near-infrared fiber probe laser that was operated with femtosecond pulses led to an increase in SNR compared to a continuous-wave laser. In a phenomenological model for the SNR an asymptotic limit for the SNR was derived that provides a metric for the best possible system performance independent. Photothermal imaging on tumor tissue was shown and the potential to provide critical insights into disease diagnosis based on biochemical structural and spatially localized morphology was outlined.

ACKNOWLEDGEMENTS

We would like to thank J. Wu, S. Tabassum, Dr. D. Roblyer, and Dr. D. J. Waxman from Boston University and the Boston University School of Medicine for providing the tumors used in these experiments. We thank K. Parsley and Dr. T. Gardner at Boston University for fixation and sectioning of the tumors.

REFERENCES

[1] Long, M. E., Swofford, R. L., Albrecht, A. C., "Thermal lens technique: a new method of absorption spectroscopy," Science **191**(4223), 183–185 (1976).

[2] Bialkowski, S. E., "Photothermal Spectroscopy Methods for Chemical Analysis," Wiley, New York (1996).

[3] Lu, S., Min, W., Chong, S., Holtom, G. R., Xie, X. S., "Label-free imaging of heme proteins with two-photon excited photothermal lens microscopy," Appl. Phys. Lett. **96**(11), 113701 (2010).

[4] Cognet, L., Tardin, C., Boyer, D., Choquet, D., Tamarat, P., Lounis, B., "Single metallic nanoparticle imaging for protein detection in cells," Proc. Natl. Acad. Sci. **100**(20), 11350–11355 (2003).

[5] Lasne, D., Blab, G. A., De Giorgi, F., Ichas, F., Lounis, B., Cognet, L., "Label-free optical imaging of mitochondria in live cells," Opt Express **15**(21), 14184–14193 (2007).

[6] Gaiduk, a., Yorulmaz, M., Ruijgrok, P. V., Orrit, M., "Room-Temperature Detection of a Single Molecule's Absorption by Photothermal Contrast," Science **330**(6002), 353–356 (2010).

[7] Yorulmaz, M., Nizzero, S., Hoggard, A., Wang, L.-Y., Cai, Y.-Y., Su, M.-N., Chang, W.-S., Link, S., "Single-Particle Absorption Spectroscopy by Photothermal Contrast," Nano Lett. **15**(5), 3041–3047 (2015).

[8] Faist, J., Capasso, F., Sivco, D. L., Sirtori, C., Hutchinson, A. L., Cho, A. Y., "Quantum Cascade Laser," Science **264**(5158), 553–556 (1994).

[9] Capasso, F., Gmachl, C., Paiella, R., Tredicucci, A., Hutchinson, A. L., Cho, A. Y., "New frontiers in quantum cascade lasers and applications," IEEE J. Sel. Top. Quantum Electron.(6), 931–947 (2000).

[10] Yeh, K., Kenkel, S., Liu, J.-N., Bhargava, R., "Fast Infrared Chemical Imaging with a Quantum Cascade Laser," Anal. Chem. **87**(1), 485–493 (2015).

[11] Farahi, R. H., Passian, A., Tetard, L., Thundat, T., "Pump–probe photothermal spectroscopy using quantum cascade lasers," J. Phys. Appl. Phys. **45**(12), 125101 (2012).

[12] Mertiri, A., Altug, H., Hong, M. K., Mehta, P., Mertz, J., Ziegler, L. D., Erramilli, S., "Nonlinear Midinfrared Photothermal Spectroscopy Using Zharov Splitting and Quantum Cascade Lasers," ACS Photonics **1**(8), 696–702 (2014).

[13] Mërtiri, A., Jeys, T., Liberman, V., Hong, M. K., Mertz, J., Altug, H., Erramilli, S., "Mid-infrared photothermal heterodyne spectroscopy in a liquid crystal using a quantum cascade laser," Appl. Phys. Lett. **101**(4), 044101-1-044101-4 (2012).

[14] Pfeifer, M., Ruf, A., Fischer, P., "Indirect absorption spectroscopy using quantum cascade lasers: mid-infrared refractometry and photothermal spectroscopy," Opt. Express **21**(22), 25643 (2013).

[15] Furstenberg, R., Kendziora, C. A., Papantonakis, M. R., Nguyen, V., McGill, R. A., "Chemical imaging using infrared photothermal microspectroscopy," SPIE Proc. **8374**, 837411–837411 – 10 (2012).

[16] Max Diem, S. B.-W., "Infrared Spectroscopy of Cells and Tissues: Shining Light Onto a Novel Subject," Appl. Spectrosc. **53**(4), 148–161 (1999).

[17] Fernandez, D. C., Bhargava, R., Hewitt, S. M., Levin, I. W., "Infrared spectroscopic imaging for histopathologic recognition," Nat. Biotechnol. **23**(4), 469–474 (2005).

[18] Bhargava, R., "Towards a practical Fourier transform infrared chemical imaging protocol for cancer histopathology," Anal. Bioanal. Chem. **389**(4), 1155–1169 (2007).

[19] Diem, M., Mazur, A., Lenau, K., Schubert, J., Bird, B., Miljković, M., Krafft, C., Popp, J., "Molecular pathology via IR and Raman spectral imaging," J. Biophotonics **6**(11-12), 855–886 (2013).

[20] Miller, L. M., Bourassa, M. W., Smith, R. J., "FTIR spectroscopic imaging of protein aggregation in living cells," Biochim. Biophys. Acta BBA - Biomembr. **1828**(10), 2339–2346 (2013).

[21] Bellisola, G., Sorio, C., "Infrared spectroscopy and microscopy in cancer research and diagnosis," Am. J. Cancer Res. **2**(1), 1–21 (2011).

[22] Berciaud, S., Lasne, D., Blab, G. A., Cognet, L., Lounis, B., "Photothermal heterodyne imaging of individual metallic nanoparticles: Theory versus experiment," Phys. Rev. B **73**(4), 45424 (2006).

[23] H. Byun, M. Y. Sander, A. Motamedi, H. Shen, G. S. Petrich, L. A. Kolodziejski, E. P. Ippen, and F. X. Kartner, "Compact, stable 1 GHz femtosecond Er-doped fiber lasers," Appl. Opt. **49**, 5577–5582 (2010).

[24] Liu, H., Totachawattana, A., Mërtiri, A., Hong, M. K., Gardner, T., Erramilli, S., Sander, M. Y., "Mid-IR photothermal imaging with a compact ultrafast fiber probe laser," 2014, SPIE Proc. 919808–919808 – 6,

[25] Babkov, L. M., Gnatyuk, I. I., Trukhachev, S. V., "Investigation of 4′-n-alkyl-4-cyanobiphenyls structure features by IR spectroscopy methods," J. Mol. Struct. **744–747**, 425–432 (2005).

[26] Eldridge, W. J., Meiri, A., Sheinfeld, A., Rinehart, M. T., Wax, A., "Fast wide-field photothermal and quantitative phase cell imaging with optical lock-in detection," Biomed. Opt. Express **5**(8), 2517 (2014).